Article:

Mohamad, D.K., Freestone, B., Masters, R.C. et al. (4 more authors) (2017) Optimized organometal halide perovskite solar cell fabrication through control of nanoparticle crystal patterning. Journal of Materials Chemistry C, 5 (9). pp. 2352-2359. ISSN 2050-7526

https://doi.org/10.1039/C6TC05189H

Journal Name

ARTICLE

Optimized organometal halide perovskite solar cell fabrication through control of nanoparticle crystal patterning

Received 00th January 20xx,
Accepted 00th January 20xx

DOI: 10.1039/x0xx00000x

www.rsc.org/

D. K. Mohamad[a], B. G. Freestone[a], R. Masters[b], M. Reinhardt[c], S. Canning[d], C. Rodenburg[b] and D. G. Lidzey[1]*

The addition of Hydrogen Iodide to organometal halide perovskite precursor solution at 1% by volume leads to a significant enhancement in average power conversion efficiency (PCE) in inverted solar cell devices, increasing from 7.7% to 11.9% and 6.1% to 10.0% in spin-cast and spray-cast devices respectively. We directly attribute this improved device performance to increased thin-film surface coverage coupled with higher optical density. X-ray diffraction studies also reveal that the HI additive facilitates full conversion of the precursor material to the crystalline perovskite phase. From solution studies, we relate these changes in device performance to the presence and distribution of precursor aggregates that effectively pattern the formation of perovskite crystals during film formation.

Introduction

Organometal halide perovskites are fascinating materials with great implications for optoelectronics. Their combination of high charge-carrier mobility, efficient light absorption and compatibility with low-temperature solution-based processes makes them particularly suited to photovoltaic applications in perovskite solar cells (PSCs). Since the early work of Kojima *et al.*[1], recent research efforts have seen their power conversion efficiencies (PCEs) rise from 3.8% to 22.1%[2] in state-of-the art devices.

Conventionally, PSC active layers are deposited from a precursor solution of that is most commonly composed of a blend of lead halides and methyl ammonium halides. After casting the precursor solution to create a thin-film, thermal annealing results in the formation of a polycrystalline perovskite crystal film. Managing this process is key to producing high-efficiency PSCs as their performance is very sensitive to active layer microstructure and crystal purity. To address this issue, solution additives including water[3, 4], Hydrogen Iodide (HI)[5-7], alkyl halides[8, 9] and chloronaphthalene[10] have all been shown (when added in the correct concentration), to enhance PSC device efficiency by controlling the perovskite crystallisation kinetics through modulation of lead salt solubility and solvent drying rate.

In this study, we focus on the well characterised $PbCl_2$:MAI precursor ink formulation which is used in the single-step deposition of $MAPbI_{3-x}Cl_x$ perovskite thin-films in planar PSC device architectures[11, 12]. Critically, we explore two different techniques to deposit the $PbCl_2$:MAI precursor; spin-coating and spray-coating. While spin-coating has been the method of choice to fabricate PSCs, there is growing interest in the use of spray-coating[13-16] as it presents a ready means for possible manufacture scale-up[17]. Through careful optimisation of PSC fabrication conditions, we show addition of 1% by volume (v%) of HI to the perovskite precursor solution has a marked positive effect on device behaviour; an observation that applies to PSCs prepared both by spin-casting and spray-casting. Previous work by Heo *et al.*[6] demonstrated that by adding HI at 9.1 v% to a 1:1 PbI_2:MAI precursor ink facilitates single-step deposition of a continuous $MAPbI_3$ film without pinholes or impurities, leading to devices having a remarkably high PCE (17.2% average). These authors attributed such effects to the enhanced solubility of $MAPbI_3$ that favours the growth of a continuous perovskite crystal during the film formation process. Furthermore, it was suggested that the HI facilitated a recovery of decomposed MAI, resulting in the complete consumption of PbI_2 and thus the formation of a pure perovskite crystal.

Rather than the rapid perovskite crystal formation during film casting typical of single halide systems, mixed halide ink systems rely on extended thermal treatments to convert the precursor to the final perovskite form[18, 19]. In such systems, the crystal formation dynamics are distinctly different and thus require another set of processing conditions for the fabrication of efficient PSCs. In order to better understand our results, we employ thin-film absorption, PL emission, scanning electron microscopy (SEM) and X-ray diffraction (XRD) to explore film structure. From our XRD patterns, we conclude that when added at 1% by volume, the HI additive facilitates full conversion of precursor material leading to a pure crystalline

---

[a] Department of Physics and Astronomy, The University of Sheffield, Hicks Building, Hounsfield Road, Sheffield S3 7RH, U.K. email: d.g.lidzey@sheffield.ac.uk
[b] Department of Materials Science and Engineering, The University of Sheffield, Mappin Street, Sheffield S1 3JD, U.K.
[c] Ossila Ltd., Kroto Innovation Centre, Broad Lane, Sheffield, S3 7HQ, U.K.
[d] Department of Chemistry, University of Sheffield, Sheffield S3 7HF, U.K.

† Electronic Supplementary Information (ESI) available: See DOI: 10.1039/x0xx00000x

perovskite phase. In addition, our measurements also suggest an increased lattice spacing that is consistent with an observed red-shift in the onset of absorption and PL. SEM images and optical absorption spectra confirm that thin-films processed from the additive-containing precursor solutions show enhanced surface coverage which further enhances PCE. At higher HI concentrations however, we observe a reduction in device efficiency that appears correlated with the formation of large, disconnected crystallites and poor film coverage. Our measurements confirm therefore that precise control over the composition of the precursor ink is necessary to optimise the structure and performance of the final perovskite film.

Results and Discussion

We fabricated a series of devices based on the generic structure ITO/PEDOT:PSS/ MAPbI$_{3-x}$Cl$_x$/LiF/Al, where the active perovskite film was deposited from a MAI:PbCl$_2$ (2.9:1.0) precursor solution in DMF containing HI at 1 v%, with films being subsequently annealed at 90ºC for 90 minutes. Here, both spin-coating and spray-coating were used to deposit the MAI:PbCl$_2$ precursor – *see* Experimental Methods for full ink formulation and device fabrication details. We summarise performance metrics of devices containing a spin-cast and spray-cast active layer in Table 1. It can be seen that by adding HI to the precursor ink, there is a marked enhancement in device performance in both spin-cast and spray-cast devices with PCE increasing from 7.7% to 11.9% and 6.1% to 10.0% respectively. This is exemplified in Fig. 1(a) and (b) where we plot PCE histograms for spin-cast and spray-cast devices respectively (data recorded from devices containing the HI additive is plotted in red). For completeness, we also plot J-V traces from champion PSCs deposited by spin- and spray-casting in Fig. 1(c). Our analysis clearly demonstrates that the observed improvement in device performance is statistically significant.

In a 1 v% HI precursor film we find that the majority of this efficiency improvement results directly from an increase in the J_{SC}, although small increases in V_{OC} and FF are observed as well. We have in fact explored a range of HI concentrations as shown in Fig. 1(d). Here it is evident that 1 v% represents an optimum HI additive concentration for both device fabrication methods, although it is clear that the spin-cast devices have higher peak and average efficiency in general than the analogous spray-cast devices. This disparity arises from reduced active-layer uniformity and the fact that these films require thicker layers of PCBM to effectively planarise them[20]. Above an optimum 1 v% HI concentration, we find a dramatic roll-off in PSC device performance that results from significant reductions in FF, J_{sc} and V_{oc} (see Fig. S3 and S4). To explore

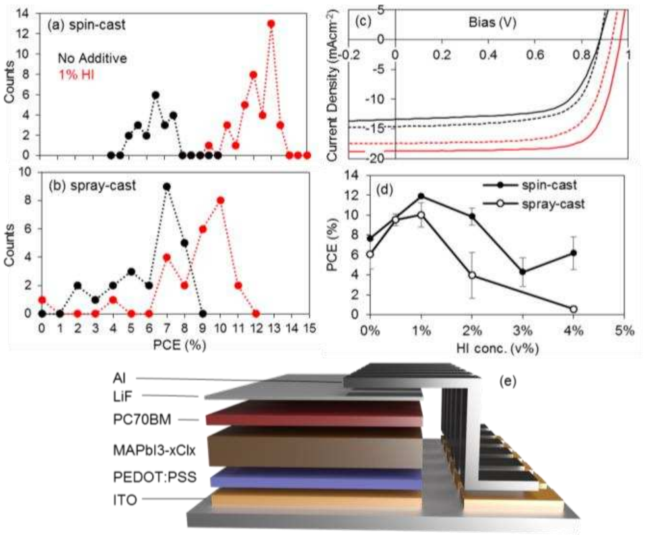

Fig. 1 – PSC device performance summary: PCE histograms of PSCs prepared by spin-casting (part (a)) and spray-casting (part (b)) perovskite precursor inks without (black circles) and with (red circles) the HI additive; Part (c) shows JV traces measured from spin-cast (solid lines) and spray-cast (dashed lines) champion cells with and without HI additive (red and black lines) under 1 Sun simulated AM1.5G irradiation. Part (d) shows the results of HI additive v% tuning experiments with spin-cast (closed circles) and spray-cast (open circles) films (Note: lines are a guide to the eye). A device structure schematic is shown in part (e).

	Spin-cast		*Spray-cast*	
Metric	No Additive	1 v% HI Additive	No Additive	1 v% HI Additive
PCE (%)	**6.7** (7.7) ± 0.9	**12.5** (13.8) ± 0.9	**6.1** (8.7) ± 1.5	**10.0** (11.4) ± 1.2
FF (%)	**58** (66) ± 8.8	**71** (77) ± 3.6	**65** (68) ± 2.2	**67** (70) ± 3.3
J_{SC} (mAcm^{-2})	**14.1** (17.2) ± 1.3	**19.3** (22.6) ± 1.4	**12.8** (14.6) ± 1.3	**17.0** (17.4) ± 0.8
V_{OC} (V)	**0.82** (0.88) ± 0.07	**0.91** (0.97) ± 0.03	**0.73** (0.88) ± 0.10	**0.88** (0.93) ± 0.06

Table 1 – Performance metrics of PSC devices measured under 1 Sun simulated AM1.5G irradiation after 10 mins light soaking. Average values are expressed in bold, champion metrics in parenthesis and the spread in metrics is represented by the standard deviation.

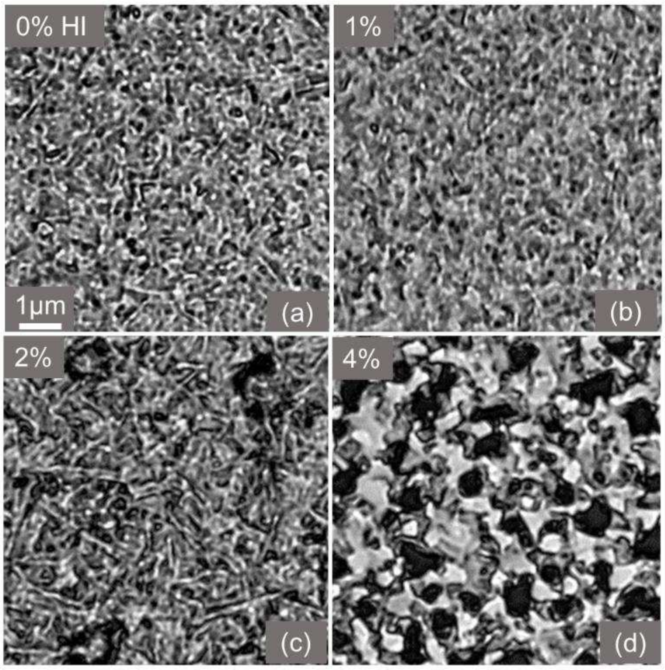

Fig. 2 – White light microscope images taken in reflection mode showing the development of PEDOT:PSS/MAPbI$_{3-x}$Cl$_x$ thin-film microstructure upon increasing precursor ink HI v% from 0% (part (a)) up to 4% (part (d)). A 1 µm scale bar is shown inset.

the origin of this reduction, we used white light reflection microscopy to characterise PEDOT:PSS/$MAPbI_{3-x}Cl_x$ thin films (post anneal) that were cast using different initial concentrations of HI (see Fig. 2(a) to (d)). Here, it can be seen that films containing 0 v% and 1 v% of HI appear relatively compact, however as the HI concentration is increased, the film is increasingly characterised by large, disconnected crystallites having poor surface coverage. This reduction in surface coverage is correlated with a progressive reduction in thin-film optical density as shown in Fig. S5(a) and (b), suggesting that reduced light harvesting ability plays a role in reducing device efficiency. It is apparent however that the addition of 1 v% HI to the precursor solution enhances the performance of devices fabricated by spin- and spray-casting, and underlines the importance of this finding as a transferrable method for controlling perovskite crystallisation dynamics and promoting high PCE.

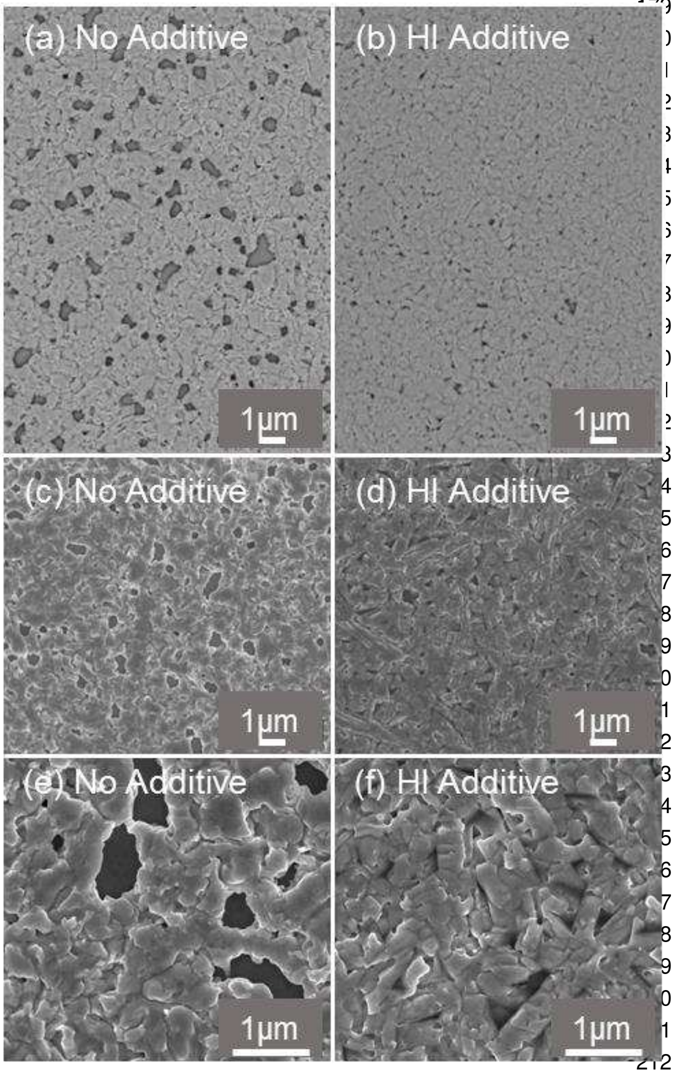

Fig. 3 – SEM images of ITO/PEDOT:PSS/$MAPbI_{3-x}Cl_x$ thin-films spin-cast from additive-free (parts (a), (c), (e)) and additive-containing (parts (b), (d), (f)) precursor solutions imaged with different detectors and at different magnifications, respectively: (a) and (b) are backscattered electron (BSE) images, with (c) to (f) being secondary electron (SE) images. A 1 µm scale-bar is shown inset.

To further explore the role of the HI precursor additive on modifying perovskite film-structure, we have used scanning electron microscopy (SEM) to explore $MAPbI_{3-x}Cl_x$/PEDOT:PSS films at higher resolution as shown in Fig. 3. Here, we compare films cast from solutions without (Fig. 3 (a), (c), (e)) and with a 1% HI additive (Fig. 3 (b), (d), (f)) at comparable thickness (*see* Table S1). In all figures, the darkest areas correspond to gaps in the film that are most clearly identified in the back-scattered electron (BSE) images as shown in Fig. 3 (a) and (b). From the latter it is immediately clear that the film cast from the precursor containing the 1 v% HI additive forms a more continuous layer and has a significantly increased surface coverage, being 93.8% (no additive) and 99.7% with 1 v% HI additive. We believe this increase in film coverage is partially responsible for the observed increase in PSC photocurrent due to the enhanced optical absorption in these films. However it is also likely that in devices processed without the HI additive, uncovered regions of PEDOT:PSS form a Schottky junction with the overlying PCBM with a V_{OC} ~ 0.5V leading to an overall reduction in cell V_{OC}[21]. The SE images (*see* Fig. 3(c) to (f), reveal the individual grains from which we determine the average size of the crystallites in films cast from additive-free precursor inks is 36% smaller than films cast without the HI additive (527 ± 20 and 385 ± 19 nm respectively). These findings are in agreement with morphological studies of such samples[22-24]. From the lower magnification images (Fig. 3(c) and (d)) it as apparent that films cast from the precursor containing the HI additive show strong local morphology variations and contain two distinctly different morphologies: (1) rounded and (2) elongated crystallites. The latter is absent in the film cast from the precursor without the HI additive. In the higher magnification images of both materials (Fig. 3 (e) and (f)) it becomes clear that smaller grains are located on top of rather larger grains. All of the above observations are consistent with a model proposed by Williams *et al.*[25], that explains the morphological variations in $MAPbI_{3-x}Cl_x$ films as a result of templated topotactic self-assembly in the presence of chloride. In this model the larger rectangular structures in Fig. 3(d) and 3(f) are suggested to result from the rapid growth of $MAPbCl_3$ present only in films cast from fresh solutions containing $PbCl_{2,}$ linked to subtle variations in chloride concentration due to aggregation in the solution[25]. We note the absence of such rectangular features in films cast from solutions without the HI additive (Fig. 3(c) and 3(e)) and speculate that it is related to the nature of aggregates in the additive-free solutions as discussed further below. Thus, the addition of HI to the precursor solution has a strong influence on the perovskite crystallisation dynamics and thus the resultant morphology of the converted perovskite thin-film.

In Fig. 4(a) we plot the optical absorption spectra of spin-cast perovskite films cast with and without the HI additive (1%) deposited onto an ITO/PEDOT:PSS substrate. It is found that there is a clear increase in optical density (by 6%) across the entire spectrum resulting from the addition of HI to the precursor solution. Given that these films are of comparable thicknesses, this increase in absorption may be accounted for

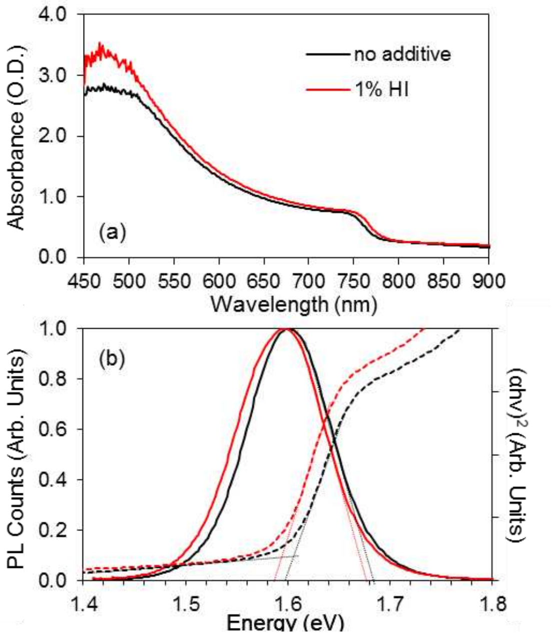

Fig. 4 – Optical spectroscopy of spin-cast ITO/PEDOT:PSS/$MAPbI_{3-x}Cl_x$ thin-films prepared from precursor solutions without (black line) and with (red line) a 1 v% HI-additive. Part (a) plots steady-state optical absorption spectra. Part (b) shows steady-state PL spectra (left-axis) with a Tauc plot (right-axis) showing absorption data.

by an increase in surface coverage across the active layer, a fact that is supported by SEM images shown in Fig. 3(a) and (b). However, since this disparity lies within the error of our profilometry measurement, we cannot rule out a simple change in thickness between samples being responsible for the observed increase in optical density. Interestingly, the absorption onset is also is red-shifted by 13 meV in the 1 v% additive-containing films as can be seen in the Tauc plot shown in Fig. 4(b). This red-shift in absorption onset is accompanied by a similar red-shift in PL emission as is also shown in 3(b) which is believed to result from enhanced perovskite crystal growth[10].

In Fig. 5, we present XRD patterns recorded from films cast from precursor solutions both with and without a 1 v% HI additive onto an ITO/PEDOT:PSS surface. An uncoated ITO/PEDOT:PSS control sample is also shown for reference, as it appears that many features in the XRD patterns arise from this substrate. We see a small feature at 23.8° (‡) which has been assigned to the mixed halide $MAPbI_{3-x}Cl_x$ perovskite cubic phase[26]. Peaks associated with the $MAPbI_3$ perovskite are marked using an asterisk (*) and are located at 14.3, 28.6, 32.0, 43.4° (tetragonal $I4/mcm$ (β) phase)[27]. All of these peaks are more intense and shifted to smaller angles in films cast using the HI additive. This result suggests that the perovskite lattice spacing increases from 6.18 to 6.19Å in response to the addition of HI to the precursor ink; a result also consistent with red-shifted absorption and PL onsets shown in Fig. 4(b). A change in composition, possibly due to differences in chlorine concentration may explain this effect in terms of lattice distortion[28]. Furthermore, we find an absence of peaks associated with the intermediate perovskite reaction product, marked with a dagger (†) at 15.7 and 31.7°[28] and PbI_2 at 12.8°[27] suggesting that the addition of HI to the precursor solution facilitates full conversion of the precursor to perovskite crystal phase.

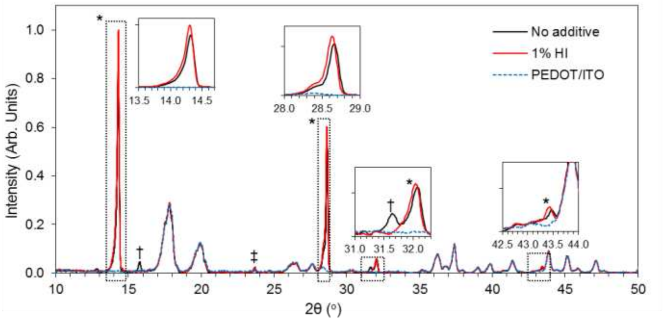

Fig. 5 – X-ray diffractograms of representative ITO/PEDOT:PSS/$MAPbI_{3-x}Cl_x$ thin-films spin-cast from a precursor solution without (black lines) and with a 1v% HI-additive (red lines) precursor solutions. Data recorded on an uncoated ITO/PEDOT:PSS substrate is shown for comparison using a dashed blue line. Regions marked with boxes are shown expanded in the insets. Features assigned to the perovskite crystal and intermediate phase are marked with * and † respectively. ‡ refers to the mixed halide cubic phase.

Finally, we turn out attention to the effect of HI in the context of solution engineering and present the results of these studies in Fig. 6. After ink preparation, we find that perovskite precursor inks appear turbid indicating the presence of unsolvated precursor materials. In Figure 6(a) to (c) we demonstrate that by adding small quantities of HI, we effectively eliminate these suspended particles leading to the formation of a clear solution. This observation is supported by the dramatic reduction in dynamic light scattering (DLS) count rate after HI addition. This measurement confirms that on addition of HI, there is (i) a large reduction in solution turbidity, and (ii) a change in the average particle size. Indeed, without the presence of HI, the solution contains a significant population of micron-sized crystallites (1370 ± 480 nm). On addition of 1 v% HI, these are apparently absent, and are replaced by a population of nanoparticles having a diameter of 1.7 ± 0.4 nm (*see* Fig S6(a) and (b)). We note that Williams *et al.*[25] have also detected the presence of 40 nm diameter aggregates in this precursor ink formulation. Note that owing to difficulties associated with effectively separating the aggregates from their parent solutions without significantly altering them, we restrict our investigation to comparative studies of precursors in solution as shown in Fig. 6. Given the large disparity between MAI and $PbCl_2$ material solubility (*see* Fig. 6(e) and (f)), we suspect that the suspended particles are in fact undissolved $PbCl_2$ microcrystals[25, 29]. We find that mixing the precursors leads to a large increase in $PbCl_2$ solubility and gives the ink a yellow appearance implying the formation of a lead polyhalide-based soft coordination complex with corresponding red-shifted excitonic absorption[30]. However, this process alone does not appear to be sufficient to fully disrupt the cohesive forces within the $PbCl_2$ precursor and some material remains undissolved in the ink without the presence of the HI additive. It is clear therefore that HI additive has a marked effect on the $PbCl_2$ solubility. This can be evidenced in Fig. 6(g) to (i), where we show that the addition of 2% HI to a $PbCl_2$ solution just above its solubility limit in DMF (40 mg/ml) appears to solvate all the previously undissolved $PbCl_2$ solid. We find that this solvation process is accompanied by a colour change of the solution from colourless to yellow, indicative of the presence of a mixed lead-halide coordination compound.

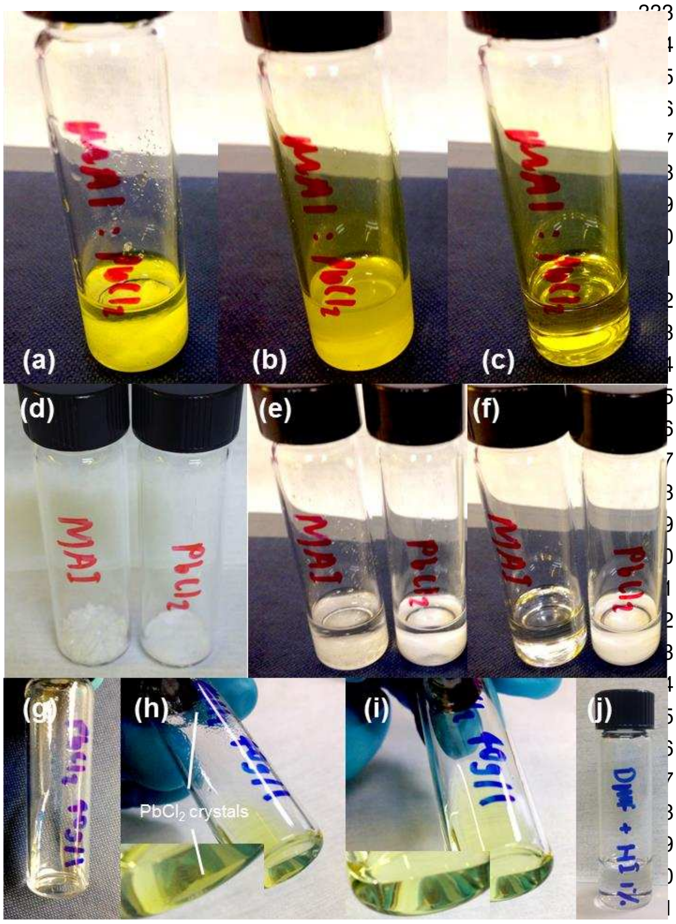

Fig. 6 – The effect of HI addition on DMF-based perovskite precursor solutions. Part (a) 2.9:1.0 MAI:$PbCl_2$ precursor ink at 500 g/l before vortex mixing, (b) after 2 mins vortex mixing and (c) after 1% HI addition and further mixing. Part (d) shows the pure MAI and $PbCl_2$ precursors before solvent is added, (e) immediately after DMF solvent addition at 312 and 188 mg/ml respectively, and (f) after extended vortex mixing. Part (g) shows pure $PbCl_2$ in DMF at 40 mg/ml after extended mixing, (h) immediately after 2% HI addition, and (i) after further vortex mixing. DMF containing 1% HI is shown for comparison in part (j).

We propose therefore that by adding HI to our mixed precursor inks, we are able to shift the dynamic solution equilibria from undissolved $PbCl_2$ microcrystallites towards a fully coordinated mixed halide complex that is readily solvated. The position of this equilibrium is expected to influence crystal microstructure through the templated self-assembly process directed by formation of the chloride-rich ($MAPbCl_3$) intermediate phase[25] or through the size and population of $PbCl_2$heterogeneous nucleation sites[29]. Both of these species have been implicated in the dynamics of film formation which is supposed to extend as far back as the solution state upon deposition[31]. In films prepared from inks without the additive, we speculate that the presence of significant amounts of $PbCl_2$ suspended in the solution as large microcrystals is likely to lead to a non-stoichiometric mixture of precursor materials that will hamper this process. It is not clear however why device efficiency is further reduced when perovskite films are cast from precursor solutions containing more than 1 v% of the HI additive. We speculate that small changes in the size or population density of chloride-rich nanoparticles (as suggested by the intensity reduction in DLS scattering signal (*see* Fig. S6(c)) will disrupt structural templating in the nascent perovskite thin-film. Indeed, changes in the population of nanoparticles able to act as nucleation sites for the growth in crystallites is likely to result in a distinct change in active-layer microstructure from a dense arrangement of elongated crystallites to one which is characterised by large disconnected crystallites and poor surface coverage. We do not expect chemical reactions between HI and precursor materials, however recovery of decomposed MAI is possible by reaction between MA and HI. We anticipate that HI will be removed from the film during the extended annealing stage and is merely added to engineer the solution for favourable device processing.

It is worth noting that our HI additive is based on a 57wt% HI solution in water. Therefore, we cannot rule out any effects associated with increasing water concentrations in our precursor inks as we add greater amounts of HI. Large concentrations of water (>3 v%) have been shown to reduce perovskite/PEDOT surface coverage due to the differing solubilities of precursors – in particular $PbCl_2$ is poorly solvated by water in contrast with MAI[3]. Such effects may alter the precursor-perovskite reaction kinetics by facilitating rapid mass transfer of MAI and by accelerating the removal of excess MAI formation of methylamine and HCl *via* acid-base interactions between MAI and water[32, 33]. Water incorporation into the perovskite lattice, as $MAPb_{3-x}Cl_x.nH_2O$ hydrate, is thermodynamically favoured and therefore expected to occur spontaneously[34]. However, the crystalline hydrate species lie beyond the detection limit of our XRD measurement (the features expected at 8.6, 11.6 and 11.7°[35, 36] appear absent). Nevertheless, the emergence of an increasing hysteresis in JV sweeps in devices processed with increasing HI v% (*see* Fig. S1-2) suggests that water may in fact be incorporated within the perovskite lattice leading to the presence of a greater concentration of mobile ions[37].

Conclusion

We have fabricated $MAPbI_{3-x}Cl_x$ photovoltaic devices based on an inverted architecture, and have explored the effect of the addition of a small volume of a hydrogen iodide additive to the precursor solution that is used to cast the device active layer. We fabricate a range of devices in which various quantities of HI were added to the precursor solution, and find that devices cast from a precursor containing 1 v% HI have enhanced power conversion efficiency (13.8% champion power conversion efficiency, (12.5 ± 0.9)% average efficiency). We propose that the HI additive has a strong effect on $PbCl_2$ solubility and therefore regulates the size and population of aggregates which are implicated in the structural templating occurring early in the film-formation process. We find a small amount (1 v%) of HI leads to the dissolution of large $PbCl_2$ microcrystals and drives the dynamic solution equilibria toward the formation of fully coordinated lead polyhalide coordination complexes which has a marked positive effect on device efficiency; an observation that is replicated in devices that are prepared by both spin-casting and spray-casting. We have used our XRD to study the structure of the perovskite films, and conclude that the HI additive facilitates full conversion of precursor material leading to a pure crystalline perovskite phase. In addition, we see an increased lattice spacing and corresponding red-shift in absorption and PL onsets. SEM images and optical absorption spectra confirm that thin-films processed from precursor solutions containing 1 v% HI additive have enhanced surface coverage which further enhances PCE.

Materials and Methods

Solar Cell Fabrication

ITO substrates ($20\ \Omega\ \square^{-1}$) purchased from Ossila Ltd were first cleaned by sonication in Helmanex solution, deionized water then isopropyl alcohol (IPA), then dried with compressed nitrogen and ozone-plasma treated before use. To deposit PEDOT:PSS by spin-coating, Clevios PVP AI4083 was first filtered through a 0.45 μm PVDF syringe filter and then spin-cast at 5000 rpm to form a 35±2 nm thick layer that was then annealed in air at 120 ºC for 10 minutes prior to use.

For spray-coating (USI prism 300), the ultra-sonic tip was held at 40 mm above the substrate surface and vibrated at 35 kHz while fluid from a coating reservoir above was fed to the tip. The ink droplets created were directed to the surface using a carrier gas whose pressure was set to 10 psi giving a wide spray pattern (ca 50 mm). At the same time, the spray head was robotically scanned a distance of 150 mm over ITO device substrates in a single pass. We also found that multiple pass spray-routines create poor quality films as they tend to re-dissolve the underlying films. Unlike airbrush techniques in which droplets contain very little solvent when they reach the surface, ultrasonic spray-cast films consist of droplets that coalesce to form a fully wet film before drying[38]. Note that the width of the spray-pattern is significantly larger than that of the individual device pixels (each having a size (2 x 2) mm^2), and thus significant heterogeneity across the spray-mist pattern at the sample surface is not anticipated. Substrates were mounted on a hotplate to ensure stable elevated temperatures in order to control the wet film drying rate.

Perovskite precursor solutions were prepared from methyl ammonium iodide (MAI, purchased from Ossila Ltd), hydrogen iodide (Sigma 210021) and $PbCl_2$ (Sigma 203572) and were used as received. Spin-coated samples were cast at a spin-speed of 4000 rpm from a 500 mg ml^{-1} 2.9:1.0 MAI:$PbCl_2$ solution containing 0 to 4v% HI in DMF (Sigma 227056). Prior to film deposition, both the substrate and casting solution were held at a temperature of 90 ºC and 70 ºC respectively to enable rapid drying of the films and to optimize device performance. Spray-cast perovskite precursor films were deposited from a 200 mg ml^{-1} 2.9:1.0 MAI:$PbCl_2$ solution in DMF containing 0 to 4v% HI (solution at ambient temperature) onto substrates held at 90 ºC with a head-speed of 220 mm s^{-1}. In all cases, film thickness was determined from post-annealed films at five locations using profilometry. Spray-coated and spin-coated film thickness was adjusted to be within 20% of each other however the addition of HI was seen to modulate this (*see* Table S1). Lab humidity was controlled with an air conditioning system and a desiccant dehumidifier (Humidity control systems Ltd DC31 T16).

The perovskite films were spin-coated with a PC$_{70}$BM electron-extraction layer (95% purity supplied by Ossila Ltd). Spin-cast films were deposited in a nitrogen-filled glove-box. PCBM solutions for spin-casting were prepared at 50 mg ml^{-1} or 70 mg ml^{-1} in chlorobenzene, creating 150 and 200 nm thick films respectively. Prior to deposition, solutions were heated to 70 ºC for 1 hour, allowed to cool and then filtered through a 0.45 μm PTFE syringe filter.

A cathode of LiF and aluminium was thermally evaporated at 2 nm at 0.1 Å s^{-1} and 100 nm at 1 Å s^{-1} respectively within a vacuum chamber held at *ca* 10^{-6} mbar. Devices were encapsulated using a UV-treated epoxy (supplied by Ossila Ltd) before testing.

Steady-state photoluminescence was performed using a Laser- LDCU CW 450nm diode laser rated at 1mW with a power density of ~0.1 W/cm^2 on the sample. All photoluminescence spectroscopy was performed under vacuum (<10^{-5} mBar). UV-vis measurements were performed under ambient conditions using UV-VIS-NIR light source (Ocean Optics – DH-2000-BAL), collection fibre optic cables (Ocean Optics) and spectrometer (Ocean Optics – HR2000+ES).

Xray diffraction

Thin-film X-ray diffraction was performed on perovskite/PEDOT:PSS/ITO glass samples using a Bruker D8 diffractometer using Cu-Kα radiation in 0.05° increments over the Bragg angle range of 10−50°.

SEM

Samples were imaged in a FEI Nova NanoSEM 450, operating at a primary beam energy of 5 keV. The through-lens detector (TLD) was used to collect images at a working distance of 5 mm with immersion lens active. For surface coverage measurements, the TLD was set to backscattered electron imaging mode in order to generate images that best emphasised any holes in the film. For crystallite size measurements the TLD was set to secondary electron mode in order to generate images that better highlighted grain boundaries.

Dynamic Light Scattering (DLS).

Perovskite precursor ink solutions were prepared under representative conditions and analysed using a Malvern Zetasizer NanoZS instrument. Data were averaged over three consecutive measurements of ten runs each. Measurements were made at 25°C.

Solar cell characterisation

Device performance was tested under ambient conditions using a Newport 92251A-1000 solar simulator (AM1.5). An NREL certified silicon reference cell was used to calibrate the integrated light-output from the simulator to 100 mW cm^{-2} at 25 ºC. Here, an aperture mask (0.025 cm^2) was placed over each solar cell to accurately define the device area and minimize absorption of stray light. PCEs were determined for a cell initially held at +1 V, swept to -1 V and back to +1V a rate of 0.4 V s^{-1}. Performance metrics are quoted from the portion of J-V sweep as the bias is swept from +1 to -1V.

Acknowledgements

This work was funded by the UK Engineering and Physical Sciences Research Council via grants EP/M025020/1 'High resolution mapping of performance and degradation mechanisms in printable photovoltaic devices', EP/J017361/1 'Supersolar Solar Energy Hub' and EP/M014797/1 'Improved Understanding, Development and Optimisation of Perovskite-based Solar Cells' and EP/N008065/1 'SEE MORE: SECONDARY ELECTRON EMISSION - MICROSCOPY FOR ORGANICS WITH RELIABLE ENGINEERING-PROPERTIES'. B.F. thanks the EPSRC for the provision of a studentship via the 'Centre for Doctoral Training in New and Sustainable PV' (EP/L01551X/1).

References

1. A. Kojima, K. Teshima, Y. Shirai and T. Miyasaka, *Journal of the American Chemical Society*, 2009, **131**, 6050-6051.
2. W. S. Yang, J. H. Noh, N. J. Jeon, Y. C. Kim, S. Ryu, J. Seo and S. I. Seok, *Science*, 2015, **348**, 1234-1237.
3. X. Gong, M. Li, X.-B. Shi, H. Ma, Z.-K. Wang and L.-S. Liao, *Advanced Functional Materials*, 2015, **25**, 6671-6678.
4. L. Ling, S. Yuan, P. Wang, H. Zhang, L. Tu, J. Wang, Y. Zhan and L. Zheng, *Advanced Functional Materials*, 2016, **26**, 5028-5034.
5. J. H. Heo, D. H. Song and S. H. Im, *Advanced Materials*, 2014, **26**, 8179-8183.
6. J. H. Heo, D. H. Song, H. J. Han, S. Y. Kim, J. H. Kim, D. Kim, H. W. Shin, T. K. Ahn, C. Wolf, T.-W. Lee and S. H. Im, *Advanced Materials*, 2015, **27**, 3424-3430.
7. P. F. Luo, W. Xia, S. W. Zhou, L. Sun, J. G. Cheng, C. X. Xu and Y. W. Lu, *Journal of Physical Chemistry Letters*, 2016, **7**, 3603-3608.
8. C.-C. Chueh, C.-Y. Liao, F. Zuo, S. T. Williams, P.-W. Liang and A. K. Y. Jen, *Journal of Materials Chemistry A*, 2015, **3**, 9058-9062.
9. P.-W. Liang, C.-Y. Liao, C.-C. Chueh, F. Zuo, S. T. Williams, X.-K. Xin, J. Lin and A. K. Y. Jen, *Advanced Materials*, 2014, **26**, 3748-3754.
10. X. Song, W. Wang, P. Sun, W. Ma and Z.-K. Chen, *Applied Physics Letters*, 2015, **106**, 033901.
11. P. Docampo, J. M. Ball, M. Darwich, G. E. Eperon and H. J. Snaith, *Nature Communications*, 2013, **4**.
12. H. P. Zhou, Q. Chen, G. Li, S. Luo, T. B. Song, H. S. Duan, Z. R. Hong, J. B. You, Y. S. Liu and Y. Yang, *Science*, 2014, **345**, 542-546.
13. S. Das, B. Yang, G. Gu, P. C. Joshi, I. N. Ivanov, C. M. Rouleau, T. Aytug, D. B. Geohegan and K. Xiao, *Acs Photonics*, 2015, **2**, 680-686.
14. J. G. Tait, S. Manghooli, W. Qiu, L. Rakocevic, L. Kootstra, M. Jaysankar, C. A. M. de la Huerta, U. W. Paetzold, R. Gehlhaar, D. Cheyns, P. Heremans and J. Poortmans, *Journal of Materials Chemistry A*, 2016, **4**, 3792-3797.
15. A. T. Barrows, A. J. Pearson, C. K. Kwak, A. D. F. Dunbar, A. R. Buckley and D. G. Lidzey, *Energy & Environmental Science*, 2014, **7**, 2944-2950.
16. Z. Liang, S. Zhang, X. Xu, N. Wang, J. Wang, X. Wang, Z. Bi, G. Xu, N. Yuan and J. Ding, *Rsc Advances*, 2015, **5**, 60562-60569.
17. F. C. Krebs, *Solar Energy Materials and Solar Cells*, 2009, **93**, 394-412.
18. J. You, Y. Yang, Z. Hong, T.-B. Song, L. Meng, Y. Liu, C. Jiang, H. Zhou, W.-H. Chang and G. Li, *Applied Physics Letters*, 2014, **105**, 183902.
19. G. E. Eperon, V. M. Burlakov, P. Docampo, A. Goriely and H. J. Snaith, *Advanced Functional Materials*, 2014, **24**, 151-157.
20. D. K. Mohamad, J. Griffin, C. Bracher, A. T. Barrows and D. G. Lidzey, *Advanced Energy Materials*, 2016.
21. Q. Wang, Y. Shao, Q. Dong, Z. Xiao, Y. Yuan and J. Huang, *Energy & Environmental Science*, 2014, **7**, 2359-2365.
22. A. T. Barrows, S. Lilliu, A. J. Pearson, D. Babonneau, A. D. F. Dunbar and D. G. Lidzey, *Advanced Functional Materials*, 2016, **26**, 4934-4942.
23. S. Lilliu, J. Griffin, A. T. Barrows, M. Alsari, B. Curzadd, T. G. Dane, O. Bikondoa, J. E. Macdonald and D. G. Lidzey, *Crystengcomm*, 2016, **18**, 5448-5455.
24. S. Lilliu, T. G. Dane, M. Alsari, J. Griffin, A. T. Barrows, M. S. Dahlem, R. H. Friend, D. G. Lidzey and J. E. Macdonald, *Advanced Functional Materials*, 2016, n/a-n/a.
25. S. T. Williams, F. Zuo, C. C. Chueh, C. Y. Liao, P. W. Liang and A. K. Y. Jen, *Acs Nano*, 2014, **8**, 10640-10654.
26. D. Y. Luo, L. M. Yu, H. Wang, T. Y. Zou, L. Luo, Z. Liu and Z. H. Lu, *Rsc Advances*, 2015, **5**, 85480-85485.
27. Z. Song, S. C. Watthage, A. B. Phillips, B. L. Tompkins, R. J. Ellingson and M. J. Heben, *Chemistry of Materials*, 2015, **27**, 4612-4619.
28. H. Yu, F. Wang, F. Xie, W. Li, J. Chen and N. Zhao, *Advanced Functional Materials*, 2014, **24**, 7102-7108.
29. Y. Tidhar, E. Edri, H. Weissman, D. Zohar, G. Hodes, D. Cahen, B. Rybtchinski and S. Kirmayer, *Journal of the American Chemical Society*, 2014, **136**, 13249-13256.
30. K. Yan, M. Long, T. Zhang, Z. Wei, H. Chen, S. Yang and J. Xu, *Journal of the American Chemical Society*, 2015, **137**, 4460-4468.
31. S. T. Williams, C. C. Chueh and A. K. Y. Jen, *Small*, 2015, **11**, 3088-3096.
32. G. E. Eperon, S. N. Habisreutinger, T. Leijtens, B. J. Bruijnaers, J. J. van Franeker, D. W. dequilettes, S. Pathak, R. J. Sutton, G. Grancini, D. S. Ginger, R. A. J. Janssen, A. Petrozza and H. J. Snaith, *Acs Nano*, 2015, **9**, 9380-9393.
33. K. K. Bass, R. E. McAnally, S. L. Zhou, P. I. Djurovich, M. E. Thompson and B. C. Melot, *Chemical Communications*, 2014, **50**, 15819-15822.
34. E. Mosconi, J. M. Azpiroz and F. De Angelis, *Chemistry of Materials*, 2015, **27**, 4885-4892.
35. J. L. Yang, B. D. Siempelkamp, D. Y. Liu and T. L. Kelly, *Acs Nano*, 2015, **9**, 1955-1963.
36. A. M. A. Leguy, Y. Hu, M. Campoy-Quiles, M. I. Alonso, O. J. Weber, P. Azarhoosh, M. van Schilfgaarde, M. T. Weller, T. Bein, J. Nelson, P. Docampo and P. R. F. Barnes, *Chemistry of Materials*, 2015, **27**, 3397-3407.

37. C. Clegg and I. G. Hill, *Rsc Advances*, 2016, **6**, 52448-52458.
38. C. Girotto, D. Moia, B. P. Rand and P. Heremans, *Advanced Functional Materials*, 2011, **21**, 64-72.